Reflection-induced spectral changes of the pulsed radiation emitted by a point source

Wiersma, S.H.; Visser, T.D.; de Hoop, A.T.

published in
Physical Review E
2001

DOI (link to publisher)
10.1103/physreve.63.046603

document version
Publisher's PDF, also known as Version of record

Reflection-induced spectral changes of the pulsed radiation emitted by a point source

S. H. Wiersma,[1] T. D. Visser,[1,*] and A. T. de Hoop[2]
[1]*Department of Physics and Astronomy, Free University, De Boelelaan 1081, 1081 HV Amsterdam, The Netherlands*
[2]*Laboratory of Electromagnetic Research, Faculty of Information Technology and Systems, Delft University of Technology, Mekelweg 4, 2628 CD Delft, The Netherlands*

(Received 22 December 1999; revised manuscript received 22 September 2000; published 21 March 2001)

We calculate the field emitted by a pulsed point source above a planar interface. It is found that the observed power spectrum can differ significantly from the emitted spectrum. Also, the observed power spectrum depends strongly on the wave speeds in the two media and on the position of the observation point with respect to the interface and the source.

DOI: 10.1103/PhysRevE.63.046603 PACS number(s): 82.80.Dx, 42.15.Dp, 42.25.Gy

I. INTRODUCTION

The power density spectrum of the wave field that is observed at a certain distance from its emitting source usually differs from that of the source excitation. Examples of this are known in the fields of optics and acoustics. There are, within the linear regime, at least five different mechanisms that can cause this. First, we mention the Doppler effect which manifests itself when the source and the observer are in relative motion [1]. Second, when a pulsed wave propagates through an absorbing medium, the interplay of dispersion and absorption (in accordance with the principle of causality) causes changes in the spectrum of the wave field [2]. Third, partially coherent sources give rise to so-called correlation-induced spectral changes [3]. A fourth, and closely related, mechanism is scattering by a random medium. An overview of the last two processes and their consequences for the wave field's power density spectrum are described in [4] and [5]. In the present paper we study a fifth cause of spectral changes, namely, reflection at an interface.

We analyze how reflection at a planar interface between two media with different wave speeds changes the spectrum of a propagating wave emitted by a pulsed point source. Our analysis is carried out in the time domain, and yields analytical expressions for the relevant Green's functions. These are convolved with the source excitation function to obtain the observed wave field. A Fourier transform then yields the observed power spectrum.

In the model configuration at hand, the primary wave field excited by the point source is a spherical wave. Its power density spectrum is, at each observation point in space, a replica of that of the exciting source. The wave reflected at the interface has a spherical wave front with its center at the image of the source in the interface, but its amplitude and pulse shape no longer show a spherical symmetry, and they change with the offsets of the point of observation parallel and normal to the interface, and with the two wave speeds. In addition, in the case where the medium against which reflection takes place has a wave speed that exceeds the one of the medium in which the wave motion is generated, head waves occur in certain regions of space. Their wave front is a conical one and their amplitude and pulse shape deviate from those of both the primary and the reflected waves. Because of the difference in pulse shape in these three constituents, their spectral contents differ, with the consequence that the power density spectrum of the total wave motion that is observed varies in a complicated fashion with the position of observation. Our analysis unravels the influence of the different parameters on this phenomenon in a quantitative manner. The results are expected to be of importance in all those cases where conclusions are drawn from the measured power spectra associated with the irradiation of an object, for example, in those cases where the process of irradiation aims at reconstructing certain parameters of the irradiated object.

As will be demonstrated, the changes in the observed power spectrum can be quite significant. Not only do our results establish interface reflection as a mechanism for spectral changes, they are also relevant for inverse scattering studies where the source excitation is to be reconstructed.

The analysis of the pulse propagation in the two-media configuration is carried out with the use of the modified Cagniard technique [6]. This method has been successfully applied in electromagnetics [7,8], acoustics [9,10], and elastodynamics [11,12]. In the present study we consider scalar wave fields. In our numerical examples, the parameters are taken from acoustics. In addition, pulse time widths are chosen such that within the spectral regime dispersion can be neglected.

Our method of analysis yields closed-form time-domain results for the generated wave motion. The analytic form of the relevant expressions has a number of advantages over results that are obtained with the aid of purely computational techniques like the finite difference time-domain (FDTD) method. First of all, the singularities in the complex slowness domain expressions for the wave field (and these govern the time behavior of the field) are each directly associated with a physical phenomenon occurring in the wave motion. Secondly, explicit expressions for the system's Green's function are obtained. Thirdly, since only integrations occur in the final expressions, the wave field can be computed with any prescribed accuracy. Fourthly, the computation time associated with evaluating the resulting (single) integral is negligible compared with the computation times associated with three-dimensional FDTD methods. These properties make the results of our method ideally suitable for benchmarking other techniques, both in accuracy and in speed of computation.

*Corresponding author. Email address: tvisser@nat.vu.nl

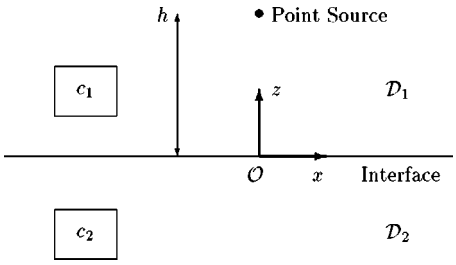

FIG. 1. A point source above a planar interface. The source is located on the z axis at a distance h from the interface between the two half spaces $\mathcal{D}_1$ and $\mathcal{D}_2$. Wave speeds in these two media are c_1 and c_2, respectively.

As far as generalizations are concerned, we mention that the modified Cagniard method also yields closed-form results for the radiation from a point source in a discretely layered medium [13] as well as in a continuously layered medium [14–16], although in the latter case the results are somewhat more complicated since reflection now takes place continuously rather than discretely. In these configurations the analysis of spectral changes can, therefore, take place along the lines of the present paper as well. Furthermore, extended sources can be handled with the same method, as experience in elastodynamic problems has shown [17].

II. DESCRIPTION OF THE CONFIGURATION

The two-media configuration under consideration consists of two half spaces $\mathcal{D}_1$ and $\mathcal{D}_2$ (see Fig. 1). To locate position in the configuration, orthogonal Cartesian coordinates $\{x,y,z\}$ with respect to a fixed reference frame are used. The reference frame is chosen such that the half space $\mathcal{D}_1$ coincides with $\{z>0\}$, and the half space $\mathcal{D}_2$ with $\{z<0\}$. The point source is located at $\{0,0,h\}$ with $h>0$. The time coordinate is t. The wave speeds in $\mathcal{D}_1$ and $\mathcal{D}_2$ are denoted by c_1 and c_2, respectively.

The scalar wave motion is described by the wave function $u=u(x,y,z,t)$. We write

$$u=\begin{cases} u_0+u_1 & \text{in } \mathcal{D}_1, \\ u_2 & \text{in } \mathcal{D}_2, \end{cases} \tag{1}$$

(2)

where u_0 denotes the wave field incident on the interface $\{z=0\}$, u_1 is the reflected wave field in $\mathcal{D}_1$, and u_2 is the transmitted wave field in $\mathcal{D}_2$. Let $f=f(t)$ be the pulse shape (''signature'') of the exciting point source; then the wave functions satisfy the following wave equations (partial differentiation is denoted by the operator ∂):

$$(\partial_x^2+\partial_y^2+\partial_z^2-c_1^{-2}\partial_t^2)u_0=-f(t)\,\delta(x,y,z-h) \quad \text{for } z>0, \tag{3}$$

$$(\partial_x^2+\partial_y^2+\partial_z^2-c_1^{-2}\partial_t^2)u_1=0 \quad \text{for } z>0, \tag{4}$$

$$(\partial_x^2+\partial_y^2+\partial_z^2-c_2^{-2}\partial_t^2)u_2=0 \quad \text{for } z<0. \tag{5}$$

We assume that $f(t)=0$ for $t<0$. Then the wave motion that is causally related to the action of the source satisfies the causality condition $u(x,y,z,t)=0$ for $t<0$ and all $\{x,y,z\}$. As the boundary conditions to be satisfied across the interface we take

$$\lim_{z\downarrow 0}[u_0(z)+u_1(z)]=\lim_{z\uparrow 0}[u_2(z)] \quad \text{for all } \{x,y\}, \tag{6}$$

$$\lim_{z\downarrow 0}[\partial_z u_0(z)+\partial_z u_1(z)]=\lim_{z\uparrow 0}[\partial_z u_2(z)] \quad \text{for all } \{x,y\}. \tag{7}$$

They are representative for the electric field components parallel to the interface in a configuration of dielectric media and the acoustic pressure in a configuration of constant volume density of mass (which implies a difference in compressibility in the two media).

The incident wave field is the spherical wave

$$u_0(x,y,z,t)=\frac{f(t-R_0/c_1)}{4\pi R_0} \quad \text{for } R_0>0, \tag{8}$$

where $R_0=[x^2+y^2+(z-h)^2]^{1/2}$.

Let

$$\hat{f}(s)=\int_0^\infty \exp(-st)f(t)dt \quad \text{for Re } (s)>0 \tag{9}$$

be the one-sided causal Laplace transformation with respect to t. Then, the power density spectrum of the source signature is

$$I_f(\omega)=10\log_{10}(|\hat{f}(i\omega)|^2), \tag{10}$$

where ω is the angular frequency, and i the imaginary unit. The diagram in which the quantity $10\log_{10}(|\hat{f}(i\omega)/\hat{f}(0)|^2)$ is plotted as a function of frequency $\omega/2\pi$ is denoted as the *spectral diagram*. Equation (8) leads to

$$\hat{u}_0(s)=\hat{f}(s)\frac{\exp(-sR_0/c_1)}{4\pi R_0} \quad \text{for } R_0>0. \tag{11}$$

Hence, the spectral diagram of the emitted wave coincides with that of the source signature. As we will show, this property no longer holds for the reflected wave u_1.

In our examples, we shall use the ''power-exponential'' modulated sinusoidal source signature [18]

$$f(t)=\begin{cases} 0 & \text{for } t<0, \\ A\left(\dfrac{\alpha t}{\nu}\right)^\nu \exp(-\alpha t+\nu)\sin(\omega_0 t) & \text{for } t\geqslant 0, \end{cases} \tag{12}$$

where A is the amplitude of the pulse and $\omega_0>0$ the angular frequency of its sinusoidal carrier, while the parameters $\alpha>0$ and $\nu>0$ are related to the pulse rise time t_r and the pulse time width t_w of the modulating amplitude function (envelope) via

$$t_r=\nu/\alpha, \tag{13}$$

$$t_w=\alpha^{-1}\nu^{-\nu}\exp(\nu)\Gamma(\nu+1), \tag{14}$$

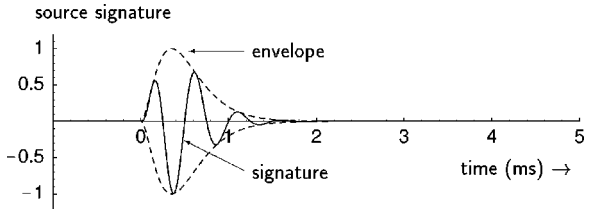

FIG. 2. Source signature or pulse shape as given by Eq. (12) (solid line) and its envelope (dashed line). Source parameters are $A=1$, $\alpha=5.71\times10^3$ s^{-1}, $\nu=2$, and $\omega_0/2\pi=2$ kHz. Corresponding pulse rise time and time width are $t_r=0.35$ ms and $t_w=0.65$ ms.

in which Γ denotes the Euler gamma function. For this source signature, we have

$$\hat{f}(s)=A\left(\frac{\alpha}{\nu}\right)^{\nu}\exp(\nu)\frac{\Gamma(\nu+1)}{2i}\times\left[\frac{1}{(s+\alpha-i\omega_0)^{\nu+1}}-\frac{1}{(s+\alpha+i\omega_0)^{\nu+1}}\right]\quad\text{for }\mathrm{Re}(s)>0. \tag{15}$$

Figure 2 shows the shape of Eq. (12), and Fig. 3 the corresponding spectral diagram.

III. THE MODIFIED CAGNIARD METHOD

The reflection problem at hand will be solved with the aid of the modified Cagniard method. The first step in this method consists of subjecting the (causal) wave functions to a one-sided Laplace transformation with transform parameter s:

$$\hat{u}(x,y,z,s)=\int_0^{\infty}\exp(-st)u(x,y,z,t)dt. \tag{16}$$

We choose $s\in\mathcal{R}$ and large enough to ensure the existence of the right-hand side. Under this transformation $\partial_t=s$. Furthermore, the spatial Fourier representation of $\hat{u}(x,y,x,s)$ in the coordinates x and y parallel to the interface, scaled by a factor of s is given by

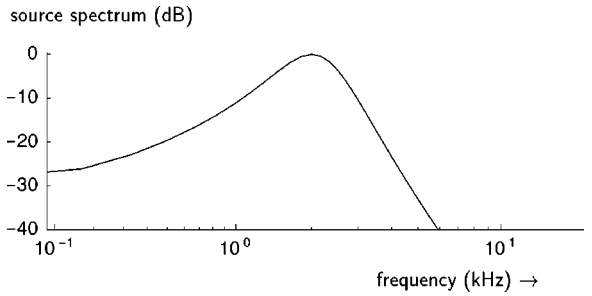

FIG. 3. Spectral diagram (normalized to 0 dB) of the source signature of Fig. 2.

$$\hat{u}(x,y,z,s)=\left(\frac{s}{2\pi}\right)^2\int_{-\infty}^{\infty}\int_{-\infty}^{\infty}\exp(-is\alpha x-is\beta y)\times\tilde{u}(\alpha,\beta,z,s)d\alpha d\beta. \tag{17}$$

In this representation, α and β are the so-called slowness parameters. With this representation, we have $\tilde{\partial}_x=-is\alpha$, $\tilde{\partial}_y=-is\beta$. As a result, the wave functions in the slowness domain satisfy the equations

$$\partial_z^2\tilde{u}_0-s^2\gamma_1^2\tilde{u}_0=-\hat{f}(s)\,\delta(z-h)\quad\text{for }z>0, \tag{18}$$

$$\partial_z^2\tilde{u}_1-s^2\gamma_1^2\tilde{u}_1=0\quad\text{for }z>0, \tag{19}$$

$$\partial_z^2\tilde{u}_2-s^2\gamma_2^2\tilde{u}_2=0\quad\text{for }z<0. \tag{20}$$

Here,

$$\gamma_{1,2}=(c_{1,2}{}^{-2}+\alpha^2+\beta^2)^{1/2}, \tag{21}$$

with the square root chosen such that $\gamma_{1,2}>0$ for all real values of α and β. The bounded solutions of these transformed wave equations are written as

$$\tilde{u}_0(\alpha,\beta,z,s)=\frac{\hat{f}(s)}{2s\gamma_1}\exp[-s\gamma_1|z-h|]\quad\text{for }z>0, \tag{22}$$

$$\tilde{u}_1(\alpha,\beta,z,s)=\mathcal{R}(\alpha,\beta)\frac{\hat{f}(s)}{2s\gamma_1}\exp[-s\gamma_1(z+h)]\quad\text{for }z>0, \tag{23}$$

$$\tilde{u}_2(\alpha,\beta,z,s)=\mathcal{T}(\alpha,\beta)\frac{\hat{f}(s)}{2s\gamma_1}\exp[-s(\gamma_1h-\gamma_2z)]\quad\text{for }z<0, \tag{24}$$

where $\mathcal{R}(\alpha,\beta)$ and $\mathcal{T}(\alpha,\beta)$ are the interface reflection and transmission coefficients, respectively. From the application of the boundary conditions [Eqs. (6) and (7)] we obtain

$$\mathcal{R}(\alpha,\beta)=\frac{\gamma_1-\gamma_2}{\gamma_1+\gamma_2}, \tag{25}$$

$$\mathcal{T}(\alpha,\beta)=\frac{2\gamma_1}{\gamma_1+\gamma_2}. \tag{26}$$

Note, in particular, that $\mathcal{R}$ and $\mathcal{T}$ remain bounded for all real values of the slowness parameters α and β, since for the chosen value of $\gamma_{1,2}$ their denominator never vanishes. Substitution of Eqs. (22)–(24) into Eq. (17) leads to representations of $\hat{u}_0$, $\hat{u}_1$, and $\hat{u}_2$, respectively.

The idea that is central to the modified Cagniard method is to transform the Fourier representations of the reflected and transmitted wave fields [Eqs. (23) and (24)] into expressions of a particular shape such that the transformation from $\hat{u}(x,y,z,s)$ to $u(x,y,z,t)$ can be carried out by inspection.

[Note that, since s in Eq. (16) has been chosen to be real and positive, we cannot rely on Fourier's integral theorem for this purpose.] Taking into account the algebraic factors of s and $f(s)$ in the expressions (22)–(24), we aim at representations of the type

$$\hat{u}(x,y,z,s)=s\hat{f}(s)\hat{g}(x,y,z,s), \tag{27}$$

in which the system's Green's function $\hat{g}$ can be cast into the form

$$\hat{g}(x,y,z,s)=\int_{T_{\rm arr}}^{\infty}\exp(-s\tau)g(x,y,z,\tau)d\tau, \tag{28}$$

where τ is a real variable of integration. In view of Lerch's theorem [19] on the uniqueness of the one-sided Laplace transformation, the time-domain equivalent of Eq. (27) then follows as

$$u(x,y,z,t)=\begin{cases}0 & \text{for } -\infty<t<T_{\rm arr},\\ \partial_t\displaystyle\int_{T_{\rm arr}}^{t}f(t-\tau)g(x,y,z,\tau)d\tau & \text{for } T_{\rm arr}<t<\infty.\end{cases} \tag{29}$$

Evidently, $T_{\rm arr}$ can be identified as the arrival time of the relevant wave motion.

A comparison of Eq. (28) with Eqs. (17) and (22)–(24) shows that τ is related to α and β via

$$i(\alpha x+\beta y)+\gamma_1(z+h)=\tau \tag{30}$$

for the reflected wave, and

$$i(\alpha x+\beta y)+\gamma_1 h-\gamma_2 z=\tau \tag{31}$$

for the transmitted wave. As a consequence, to reach our goal we have to deviate from the real values of α and β occurring in Eq. (17), which means that analytic continuations into complex values are needed. For this, we proceed as follows. First, in Eq. (17), $\{\alpha,\beta\}$ are replaced by $\{\zeta,q\}$ via

$$\alpha=\zeta\cos(\theta)-q\sin(\theta),$$

$$\beta=\zeta\sin(\theta)+q\cos(\theta), \tag{32}$$

where $x=r\cos(\theta)$ and $y=r\sin(\theta)$ with $0\leqslant r<\infty$, $0\leqslant\theta<2\pi$. Under this transformation $\alpha^2+\beta^2=\zeta^2+q^2$ and $d\alpha d\beta=d\zeta dq$, while

$$\alpha x+\beta y=\zeta r. \tag{33}$$

Subject to Eq. (32), Eq. (17) transforms into

$$\hat{u}(x,y,z,s)=\left(\frac{s}{2\pi}\right)^2\int_{-\infty}^{\infty}dq\int_{-\infty}^{\infty}\exp(-i\zeta sr)\tilde{u}(\zeta,q,z,s)d\zeta. \tag{34}$$

Next, in the inner integral, $p=i\zeta$ is introduced as the variable of integration. This leads to

$$\hat{u}(x,y,z,s)=\frac{s^2}{4\pi^2 i}\int_{-\infty}^{\infty}dq\int_{-i\infty}^{i\infty}\exp(-psr)\tilde{u}(\zeta,q,z,s)dp. \tag{35}$$

Furthermore, Eq. (21) transforms into

$$\gamma_{1,2}(p,q)=[\Omega_{1,2}^2(q)-p^2]^{1/2} \tag{36}$$

with

$$\Omega_{1,2}(q)=(c_{1,2}{}^{-2}+q^2)^{1/2}>0. \tag{37}$$

Finally, the integrand in the integral with respect to p is continued analytically into the complex p plane, away from the imaginary axis. In this procedure, we keep $\mathrm{Re}(\gamma_{1,2})\geqslant 0$, which implies that branch cuts are introduced along $\{\mathrm{Im}(p)=0,\Omega_{1,2}\leqslant|\mathrm{Re}(p)|<\infty\}$. To arrive at expressions of the type needed in Eq. (28), we can now deform the path of integration in the complex p plane, under the application of Cauchy's theorem (which necessitates avoiding crossing the branch cuts).

In our further analysis, we will concentrate on obtaining the spectral diagram of the reflected wave in its dependence on the position of observation and on the on-axis spectral diagrams of the reflected waves as a special case.

IV. THE REFLECTED WAVE IN $\mathcal{D}_1$

On using Eqs. (23), (32), and (35) we obtain

$$\hat{u}_1(x,y,z,s)=\frac{s\hat{f}(s)}{4\pi^2 i}\int_{-\infty}^{\infty}dq\times\int_{-i\infty}^{i\infty}\exp[-s(pr+\gamma_1 H_1)]\frac{\mathcal{R}(p,q)}{2\gamma_1(p,q)}dp, \tag{38}$$

where $H_1\equiv z+h$ $(H_1>0)$ is the vertically traversed distance. The inner integration is along the imaginary axis of the complex p plane. In accordance with Eqs. (30) and (33) we deform this path of integration into the modified Cagniard path

$$pr+\gamma_1 H_1=\tau, \tag{39}$$

with τ real and positive. For a fixed value of τ, we have either two complex conjugate solutions for p or two real-valued ones. The first two are given by

$$p=\begin{cases}p_1^{BW}(r,H_1,q,\tau),\\ p_1^{BW*}(r,H_1,q,\tau),\end{cases} \tag{40}$$

where

$$p_1^{BW}=\frac{r}{r^2+H_1^2}\tau+i\frac{H_1}{r^2+H_1^2}[\tau^2-T_1^2(q)]^{1/2}\quad\text{for } T_1(q)<\tau<\infty, \tag{41}$$

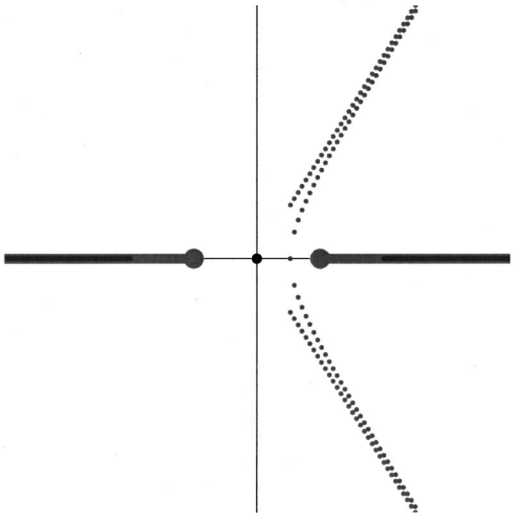

FIG. 4. Modified Cagniard path in the complex slowness plane for $c_1>c_2$. Only a body-wave contribution is present. Both the body-wave part and the asymptote are shown. Dots indicate equidistant time intervals.

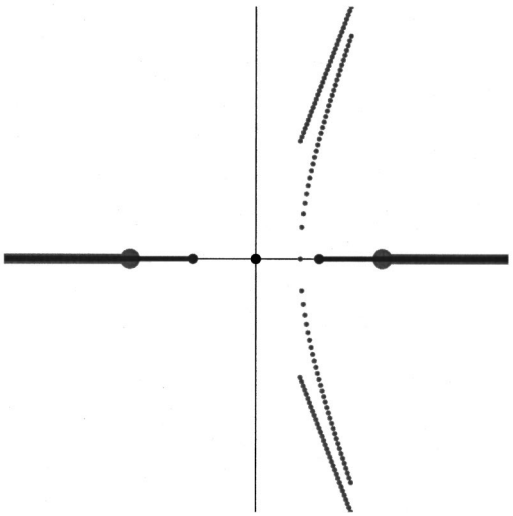

FIG. 5. Modified Cagniard path in the complex slowness plane for the case $c_2>c_1$, and no head-wave contribution. Both the body-wave part and the asymptote are shown. Dots indicate equidistant time intervals.

with

$$T_1(q)=(r^2+H_1^2)^{1/2}\Omega_1(q). \tag{42}$$

Here, the superscript BW indicates body waves. This part, the body-wave part, goes to infinity as $\tau\to\infty$ and has the asymptotic form

$$p_1^{BW}\sim\left[\frac{r+iH_1}{r^2+H_1^2}\right]\tau \quad \text{as } \tau\to\infty. \tag{43}$$

From Eq. (43) it follows that these solutions can be used to join the original path of integration (the imaginary axis) via supplementing circular arcs at infinity. In view of Jordan's lemma, the latter yield a vanishing contribution. The point of intersection of the modified Cagniard path $\{p=p_1^{BW}\}\cup\{p=p_1^{BW}*\}$ and the real p axis occurs at $\tau=T_1(q)$ and is located at

$$p=\frac{rT_1(q)}{r^2+H_1^2}. \tag{44}$$

In the case $c_1>c_2$ [where from Eq. (37) $\Omega_1(q)<\Omega_2(q)$ for all q] this point lies to the left of the left most branch point $p=\Omega_1(q)$. Since, furthermore, the integrand is free from singularities between the imaginary axis and the modified Cagniard path, the integral along the imaginary axis in Eq. (38) can be replaced by the integral along $\{p=p_1^{BW}\}\cup\{p=p_1^{BW}*\}$ (see Fig. 4).

In the case $c_1<c_2$, $\Omega_1(q)>\Omega_2(q)$ for all q, and deviations from this simple situation may occur. In this respect the part of the real axis $\{\mathrm{Im}(p)=0,-\Omega_2(q)<\mathrm{Re}(p)<\Omega_2(q)\}$ comes into play as a second candidate for the modified Cagniard path. Details of this case will be discussed below.

The case $c_1>c_2$

As was explained above, in this case the point where the p_1^{BW} contour intersects the real axis lies between 0 and the branch point $\Omega_1(q)$ as defined in Eq. (37). Therefore, in this case, only a body-wave contribution exists. Introducing τ as the variable of integration along the modified Cagniard path $\{p=p_1^{BW}\}\cup\{p=p_1^{BW}*\}$ in Eq. (38) leads to

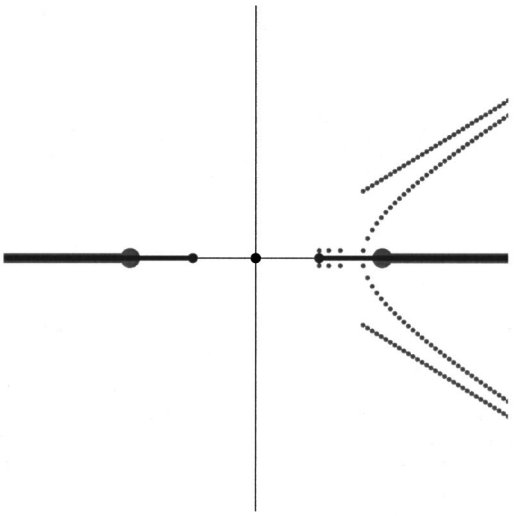

FIG. 6. Modified Cagniard path in the complex slowness plane for the case $c_2>c_1$, and a head-wave contribution. The head-wave part, the body-wave part, and the asymptote are shown. Dots indicate equidistant time intervals.

$$\hat{u}_1(x,y,z,s)=\frac{s\hat{f}(s)}{\pi^2}\int_0^\infty dq\int_{T_1(q)}^\infty \times\exp(-s\tau)\,\mathrm{Im}\left[\frac{\mathcal{R}(p_1^{BW},q)}{2\gamma_1(p_1^{BW},q)}\frac{\partial p_1^{BW}}{\partial\tau}\right]d\tau, \tag{45}$$

where we have used the facts that the integrand is an even function of q and that the integrand in p satisfies Schwarz's reflection principle of complex function theory. Interchanging the order of the integrations in Eq. (45) leads to

$$\hat{u}_1(x,y,z,s)=\frac{s\hat{f}(s)}{\pi^2}\int_{T_1(0)}^\infty d\tau \times\exp(-s\tau)\int_0^{A(\tau)}\mathrm{Im}\left[\frac{\mathcal{R}(p_1^{BW},q)}{2\gamma_1(p_1^{BW},q)}\frac{\partial p_1^{BW}}{\partial\tau}\right]dq, \tag{46}$$

from which $A(\tau)$ follows, upon using Eqs. (42) and (37) and $T_1(0)=(r^2+H_1^2)^{1/2}/c_1$, as

$$A(\tau)=\left(\frac{\tau^2}{r^2+H_1^2}-\frac{1}{c_1^2}\right)^{1/2}. \tag{47}$$

With this, we have arrived at the desired form as expressed by Eqs. (27) and (28) and the response function $g(x,y,z,\tau)$ follows from Eq. (46) by inspection as

$$g_1(x,y,z,\tau)=\begin{cases}0 & \text{for } -\infty<\tau<T_1(0),\\ \dfrac{1}{\pi^2}\displaystyle\int_0^{A(\tau)}\mathrm{Im}\left[\frac{\mathcal{R}(p_1^{BW},q)}{2\gamma_1(p_1^{BW},q)}\frac{\partial p_1^{BW}}{\partial\tau}\right]dq & \text{for } T_1(0)<\tau<\infty.\end{cases} \tag{48}$$

Substitution of this Green's function in Eq. (29) completes the solution of the reflected field for this case. Evidently, $T_1(0)$ can be interpreted as the arrival time of the wave upon traveling from the image of the point source in the interface to the point of observation in $\mathcal{D}_1$.

The case $c_1<c_2$

Now, two situations can arise, depending on the point of observation.

(a) The body-wave modified Cagniard path crosses the real p axis to the left of $\Omega_2(q)$. [Note that, since $c_2>c_1$, $\Omega_2(q)<\Omega_1(q)$; see Fig. 5.] For this case the analysis is identical with that for the previous case.

(b) The modified body-wave path ends on the real p axis on the branch cut associated with $\Omega_2(q)$. Inspection of Eq. (44) shows that this happens in the region of space

$$\Theta>\Theta_{\mathrm{crit}}=\arcsin(c_1/c_2), \tag{49}$$

where we defined

$$\sin(\Theta)=\frac{r}{(r^2+H_1^2)^{1/2}}, \tag{50}$$

with $0\leqslant\Theta<\pi/2$, and for the finite range in q given by

$$0<q<\frac{1}{\cos(\Theta)}\left(\frac{1}{c_1^2}\sin^2(\Theta)-\frac{1}{c_2^2}\right)^{1/2}=B. \tag{51}$$

[We note that Eq. (49) is the condition for total internal reflection which accompanies the occurrence of head waves.] Let $T_1^{HW}(q)$ be the value of τ corresponding to the branch point $p=\Omega_2(q)$; then

$$T_1^{HW}(q)=\Omega_2(q)r+\left(\frac{1}{c_1^2}-\frac{1}{c_2^2}\right)^{1/2}H_1, \tag{52}$$

where we used Eqs. (39) and (36). Now, the deformation of the original path of integration (the imaginary axis) into the modified Cagniard path under the application of Cauchy's theorem requires the body-wave part to be supplemented by a loop around the branch cut associated with $\Omega_2(q)$, and joining the points where the body-wave parts approach the real p axis (see Fig. 6). The parametrization of this part in accordance with Eq. (39) leads to

$$p_1^{HW}(r,H_1,\tau)=\lim_{\delta\downarrow0}\left[\frac{r}{r^2+H_1^2}\tau-\frac{H_1}{r^2+H_1^2}[T_1^2(q)-\tau^2]^{1/2}+i\delta\right] \quad \text{for } H_1\Omega_1(q)<\tau\leqslant T_1(q). \tag{53}$$

The superscript HW denotes head waves [20]. (An interesting historical account of head waves and their application in seismology is given by Mintrop [21].) The additional loop is given by $\{p=p_1^{HW}\}\cup\{p=p_1^{HW*}\}$. Introducing τ as the variable of integration in Eq. (38) gives

$$\hat{u}_1(x,y,z,s)=\frac{s\hat{f}(s)}{\pi^2}\int_0^B dq\int_{T_1^{HW}(q)}^{T_1(q)}\exp(-s\tau)\times\mathrm{Im}\left[\frac{\mathcal{R}(p_1^{HW},q)}{2\gamma_1(p_1^{HW},q)}\frac{\partial p_1^{HW}}{\partial\tau}\right]d\tau+\frac{s\hat{f}(s)}{\pi^2}\int_0^\infty dq\int_{T_1(q)}^\infty\times\exp(-s\tau)\mathrm{Im}\left[\frac{\mathcal{R}(p_1^{BW},q)}{2\gamma_1(p_1^{BW},q)}\frac{\partial p_1^{BW}}{\partial\tau}\right]d\tau, \tag{54}$$

where we have used the facts that the integrand is an even function of q and that the integrand in p satisfies Schwarz's reflection principle. As before, we interchange the order of integration, which for the head-wave contribution of Eq. (54) yields symbolically

$$\int_0^B dq\int_{T_1^{HW}(q)}^{T_1(q)}d\tau=\int_{T_1^{HW}(0)}^{T_1(0)}d\tau\int_0^{C(\tau)}dq+\int_{T_1(0)}^{D}d\tau\int_{A(\tau)}^{C(\tau)}dq, \tag{55}$$

where

$$C(\tau)=\left\{\left[\frac{\tau}{r}-\left(\frac{1}{c_1^2}-\frac{1}{c_2^2}\right)^{1/2}\frac{H_1}{r}\right]^2-\frac{1}{c_2^2}\right\}^{1/2}, \tag{56}$$

$$D=\left(\frac{1}{c_1^2}-\frac{1}{c_2^2}\right)^{1/2}\frac{(r^2+H_1^2)^{1/2}}{\cos(\Theta)}. \tag{57}$$

For the body-wave contribution of Eq. (54) we get the result obtained earlier in Eq. (46). So, finally,

$$g_1(x,y,z,\tau)=\begin{cases}0 & \text{for } -\infty<\tau<T_1^{HW}(0),\\ \frac{1}{\pi^2}\int_0^{C(\tau)}\mathrm{Im}\left[\frac{\mathcal{R}(p_1^{HW},q)}{2\gamma_1(p_1^{HW},q)}\frac{\partial p_1^{HW}}{\partial\tau}\right]dq & \text{for } T_1^{HW}(0)<\tau<T_1(0),\\ \frac{1}{\pi^2}\int_{A(\tau)}^{C(\tau)}\mathrm{Im}\left[\frac{\mathcal{R}(p_1^{HW},q)}{2\gamma_1(p_1^{HW},q)}\frac{\partial p_1^{HW}}{\partial\tau}\right]dq & \\ +\frac{1}{\pi^2}\int_0^{A(\tau)}\mathrm{Im}\left[\frac{\mathcal{R}(p_1^{BW},q)}{2\gamma_1(p_1^{BW},q)}\frac{\partial p_1^{BW}}{\partial\tau}\right]dq & \text{for } T_1(0)<\tau<D,\\ \frac{1}{\pi^2}\int_0^{A(\tau)}\mathrm{Im}\left[\frac{\mathcal{R}(p_1^{BW},q)}{2\gamma_1(p_1^{BW},q)}\frac{\partial p_1^{BW}}{\partial\tau}\right]dq & \text{for } D<\tau<\infty.\end{cases} \tag{58}$$

This concludes the calculation of the Green's function for this case. We observe that, according to Eq. (58), in the representation of $g_1(x,y,z,\tau)$ three break points in time occur. The first, $\tau=T_1^{HW}(0)$, marks the arrival time of the head waves. The second, $\tau=T_1(0)$, marks the arrival of the body wave. The third, $\tau=D$, is induced by the derivation and has no straightforward physical interpretation. Note that in the interval $T_1(0)<\tau<D$ a head-wave contribution still persists, and that in the interval $D<\tau<\infty$ only a body-wave contribution occurs.

V. THE ON-AXIS RESPONSE

For the special case that the point of observation lies on the z axis, i.e., on the line through the point source perpendicular to the interface, the analysis of the reflected field simplifies considerably and an analytic expression of the Green's function can be obtained. To see this, we substitute $x=y=0$ into Eq. (17) and use Eq. (23). This leads to

$$\hat{u}_1(0,0,z,s)=\frac{s\hat{f}(s)}{8\pi^2}\int_{-\infty}^{\infty}\int_{-\infty}^{\infty}\exp[-s\gamma_1(z+h)]\times\frac{\mathcal{R}(\alpha,\beta)}{\gamma_1(\alpha,\beta)}d\alpha d\beta. \tag{59}$$

We note that in the integrand on the right-hand side the variables α and β appear in the form $\alpha^2+\beta^2$ only. Therefore, it is now advantageous to introduce the polar variables of integration κ and ψ via

$$\alpha=\kappa\cos(\psi), \tag{60}$$

$$\beta=\kappa\sin(\psi), \tag{61}$$

with $0\leqslant\kappa<\infty$ and $0\leqslant\psi<2\pi$. This yields $d\alpha d\beta=\kappa d\kappa d\psi$, and

$$\gamma_{1,2}(\kappa)=(c_{1,2}^{-2}+\kappa^2)^{1/2}, \tag{62}$$

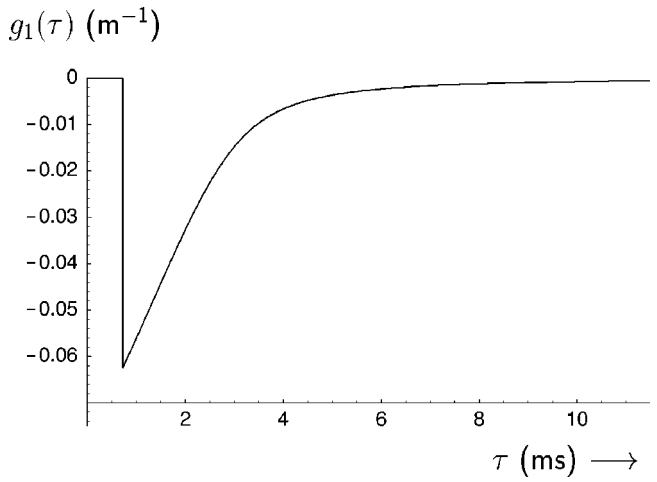

FIG. 7. Green's function $g_1(\tau)$ for the case $c_1=1500$ m/s, $c_2=330$ m/s, and the source located at $r=0$ m, $z=0.3$ m. Observation point is at $r=1.0$ m, $z=0.1$ m. Body-wave arrival time is at $\tau=0.72$ ms.

$$\mathcal{R}(\kappa)=\frac{\gamma_1(\kappa)-\gamma_2(\kappa)}{\gamma_1(\kappa)+\gamma_2(\kappa)}, \tag{63}$$

where we have used Eqs. (21) and (25). With this, Eq. (59) reduces to

$$\hat{u}_1(0,0,z,s)=\frac{s\hat{f}(s)}{4\pi}\int_0^\infty \exp[-s\gamma_1(z+h)]\frac{\mathcal{R}(\kappa)}{\gamma_1(\kappa)}\kappa d\kappa. \tag{64}$$

In order to arrive at the desired form as expressed by Eqs. (27) and (28) we carry out the transformation

$$\gamma_1(\kappa)(z+h)=\tau, \tag{65}$$

with τ real and positive. This leads to

$$\kappa^2=\frac{\tau^2}{(z+h)^2}-\frac{1}{c_1^2}. \tag{66}$$

Rewriting all functions in Eq. (64) in terms of their dependence on τ yields

$$\hat{u}_1(0,0,z,s)=\frac{s\hat{f}(s)}{4\pi}\int_{T_{\rm arr}}^\infty \exp(-s\tau)\frac{\mathcal{R}(\tau)}{z+h}d\tau, \tag{67}$$

where $T_{\rm arr}=(z+h)/c_1$. Evidently, $T_{\rm arr}$ is the arrival time of the reflected wave at the point $\{0,0,z\}$. In view of Eqs. (27)–(29) we find that the on-axis Green's function for the reflected field is now given by

$$g_1(0,0,z,t)=\begin{cases}0 & \text{for } -\infty<t<T_{\rm arr},\\ \dfrac{1}{4\pi}\dfrac{\mathcal{R}(t)}{z+h} & \text{for } T_{\rm arr}<t<\infty.\end{cases} \tag{68}$$

This result for the on-axis Green's function for the reflected field may be compared with the one that results upon substituting $r=0$ into Eq. (34), i.e.,

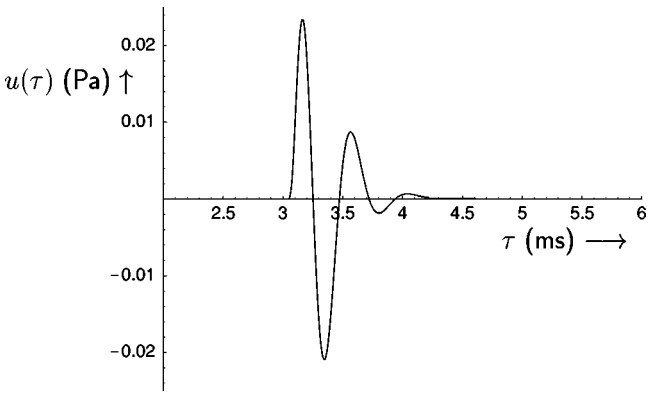

FIG. 8. Total field $u(\tau)$ for the case $c_1=500$ m/s, $c_2=330$ m/s. The source is at $r=0$ m, $z=0.3$ m. Observation point is at $r=1.5$ m, $z=0.05$ m. In this case the direct wave arrival time $T_0^{dir}=3.04$ ms and the body-wave arrival time $T_1(0)=3.08$ ms. Source parameters are $\omega_0=2\pi\times10^3$ rad s^{-1}, $\nu=2$, $\alpha=8.71\times10^3$ s^{-1}, $t_r=0.23$ ms, and $t_w=0.42$ ms.

$$\hat{u}_1(0,0,z,s)=\frac{s\hat{f}(s)}{8\pi^2}\int_{-\infty}^\infty dq\int_{-\infty}^\infty \frac{\mathcal{R}[(\zeta^2+q^2)^{1/2}]}{\gamma_1}\times\exp[-s\gamma_1(z+h)]d\zeta, \tag{69}$$

where we have expressed that $\mathcal{R}$ is a function of $(\zeta^2+q^2)^{1/2}$ only. To arrive at the form for the application of Lerch's theorem, we replace in the inner integral on the right-hand side the variable ζ by τ via

$$\gamma_1(z+h)=\tau. \tag{70}$$

This leads to

$$\zeta=\left[\frac{\tau^2}{(z+h)^2}-q^2-\frac{1}{c_1^2}\right]^{1/2}, \tag{71}$$

with the Jacobian

$$\frac{\partial\zeta}{\partial\tau}=\frac{\tau}{(z+h)^2\zeta}. \tag{72}$$

Under this transformation, Eq. (69) takes the form

$$\hat{u}_1(0,0,z,s)=\frac{s\hat{f}(s)}{2\pi^2}\int_0^\infty dq\int_{T_0(q)}^\infty \exp(-s\tau)\frac{\mathcal{R}(\tau)}{z+h}\times\left[\frac{\tau^2}{(z+h)^2}-q^2-\frac{1}{c_1^2}\right]^{-1/2}d\tau, \tag{73}$$

with

$$T_0(q)=(z+h)\left[q^2+\frac{1}{c_1^2}\right]^{1/2}. \tag{74}$$

Interchanging the order of integration, we obtain

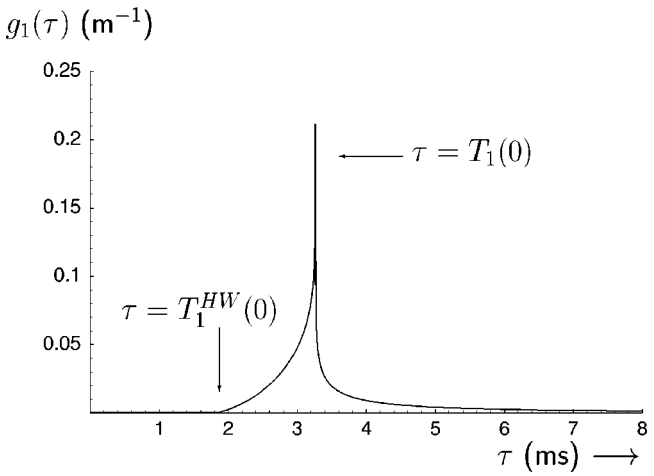

FIG. 9. Green's function $g_1(\tau)$ for the case $c_1=330$ m/s, $c_2=1500$ m/s. The source is at $r=0$ m, $z=0.3$ m. Observation point is at $r=1$ m, $z=0.1$ m. In this case head-wave arrival time $T_1^{HW}(0)=1.8$ ms and body-wave arrival time $T_1(0)=3.3$ ms.

$$\hat{u}_1(0,0,z,s)=\frac{s\hat{f}(s)}{2\pi^2(z+h)}\int_{T_{\rm arr}}^{\infty}\exp(-s\tau)\mathcal{R}(\tau)d\tau \times\int_0^{Q_0(\tau)}\{[Q_0(\tau)]^2-q^2\}^{-1/2}dq, \quad (75)$$

with

$$Q_0(\tau)=\left[\frac{\tau^2}{(z+h)^2}-\frac{1}{c_1^2}\right]^{1/2}. \quad (76)$$

Through the substitution

$$q=Q_0(\tau)\sin(\psi) \quad (77)$$

it is found that

$$\int_0^{Q_0(\tau)}\{[Q_0(\tau)]^2-q^2\}^{-1/2}dq=\int_0^{\pi/2}d\psi=\pi/2. \quad (78)$$

Hence

$$\hat{u}_1(0,0,z,s)=\frac{s\hat{f}(s)}{4\pi(z+h)}\int_{T_{\rm arr}}^{\infty}\exp(-s\tau)\mathcal{R}(\tau)d\tau, \quad (79)$$

which is the same expression as in Eq. (67), but obtained in a different manner. The Green's function time-domain result is again given by Eq. (68).

VI. NUMERICAL RESULTS

The numerical integrations and time convolutions resulting from the modified Cagniard method were carried out with the help of routines D01AJF and C06FKF of the NAG software library [22]. First we consider the case $c_1>c_2$, which implies that there are no head waves. An example of the Green's function $g_1(\tau)$ as given by Eq. (48) is shown in Fig. 7. At the body-wave arrival time $\tau=T_1(0)$ it has a jump discontinuity and then tends to zero. We note that the function is negative (positive) when $c_1>c_2$ ($c_1<c_2$), in agreement with the behavior of the reflection coefficient [Eq. (25)]. An example of the total field (i.e., the direct plus the reflected fields) $u(\tau)$ is given in Fig. 8.

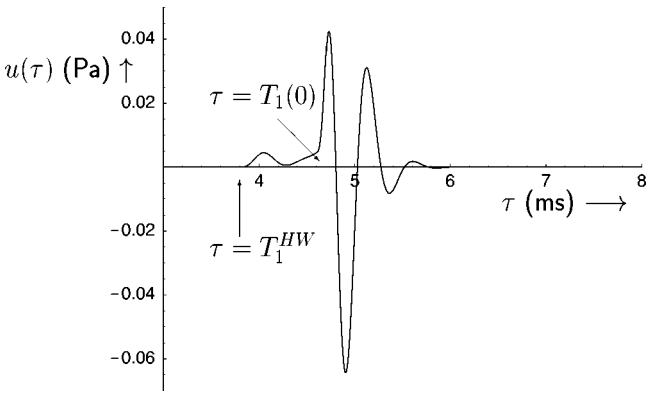

FIG. 10. Total field $u(\tau)$ for the case $c_1=330$ m/s, $c_2=500$ m/s. Source is at $r=0$ m, $z=0.3$ m. Observation point is at $r=1.5$ m, $z=0.05$ m. In this case head-wave arrival time $T_1^{HW}=3.8$ ms, direct wave arrival time $T_0^{dir}=4.6$ ms, and body-wave arrival time $T_1(0)=4.7$ ms. Source parameters are as in Fig. 8.

In the previous two examples, $c_1>c_2$. Upon interchanging the two wave speeds, head waves may occur. In that case the Green's function $g_1(\tau)$ is given by Eq. (58). An example is depicted in Fig. 9. At the head-wave arrival time $\tau=T_1^{HW}(0)$ the function is continuous and increases to a sharp maximum at the body-wave arrival time $\tau=T_1(0)$. The total field $u(\tau)$ for the case when head waves are present is depicted in Fig. 10. The contribution of the head wave is clearly visible before the arrival of the direct wave. When the point of observation is moved further away from the point source the separation between the head-wave and the body-wave contributions becomes even more distinct. The case in point is illustrated in Fig. 11.

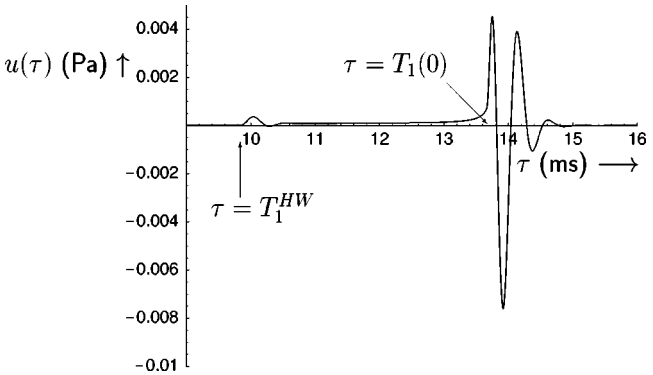

FIG. 11. Total field $u(\tau)$ for the case $c_1=330$ m/s, $c_2=500$ m/s. Source is at $r=0$ m, $z=0.3$ m. Observation point is at $r=4.5$ m, $z=0.05$ m. Notice that the head-wave contribution is separated from the body-wave contribution. In this case head-wave arrival time $T_1^{HW}=9.79$ ms, direct wave arrival time $T_0^{dir}=13.66$ ms, and body-wave arrival time $T_1(0)=13.68$ ms. Source parameters are as in Fig. 8.

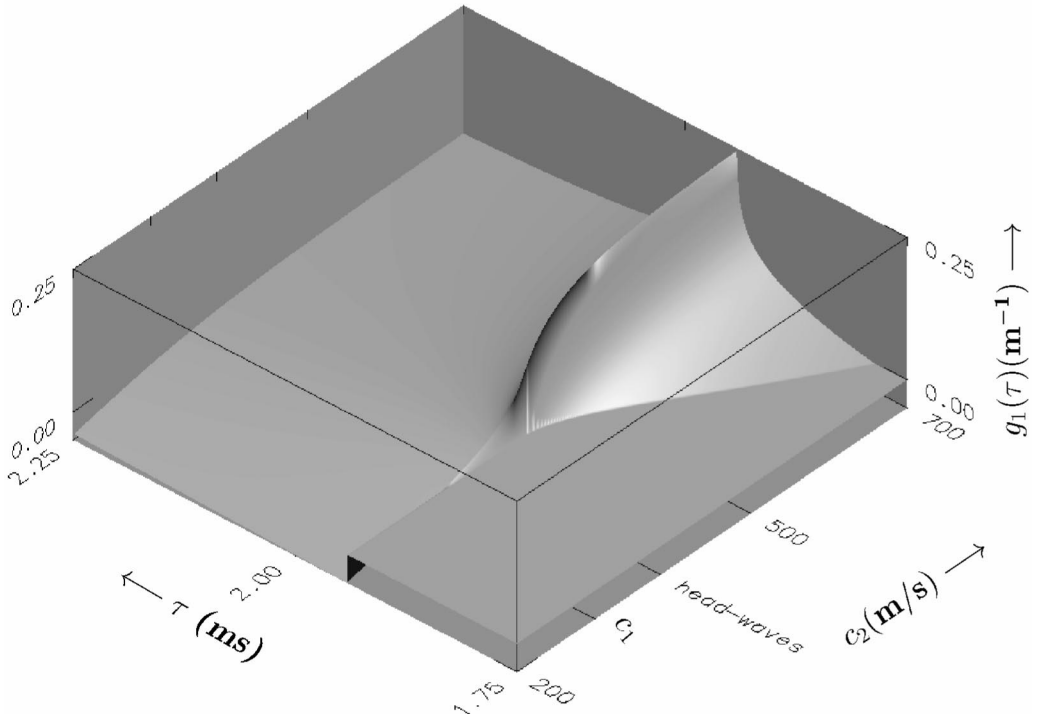

FIG. 12. Green's function at a fixed observation point as a function of time, with c_2, the wave speed in the second medium, a parameter. Source is at $r=0$ m, $z=0.3$ m. Observation point is at $r=0.5$ m, $z=0.1$ m. Wave speed in the first medium is $c_1=330$ m/s.

The transition of a Green's function of the kind given by Eq. (48) to one as given by Eq. (58) is shown in Fig. 12. Here the Green's function at a fixed point of observation is depicted as a function of time, with c_2, the wave speed in the second medium, a parameter. In the case $c_2<c_1$, the Green's function is negative and its amplitude decreases as c_2 increases. For $c_2=c_1$ it vanishes identically. For $c_2>c_1$, its sign becomes positive and its amplitude becomes larger with increasing c_2. From a certain value of c_2 onwards—at this particular observation point—head waves appear. This is accompanied by the continuous onset of the Green's function prior to the discontinuity associated with the arrival of the reflected body wave. Also, from the onset of the head waves on, its arrival time starts to decrease with increasing c_2.

An example of the extent of the direct and reflected wave fronts in the half space $\mathcal{D}_1$ as calculated with Eqs. (29) and (58) is shown in Fig. 13. It is noted that the direct wave has a spherical wave front, whereas the head wave has a conical

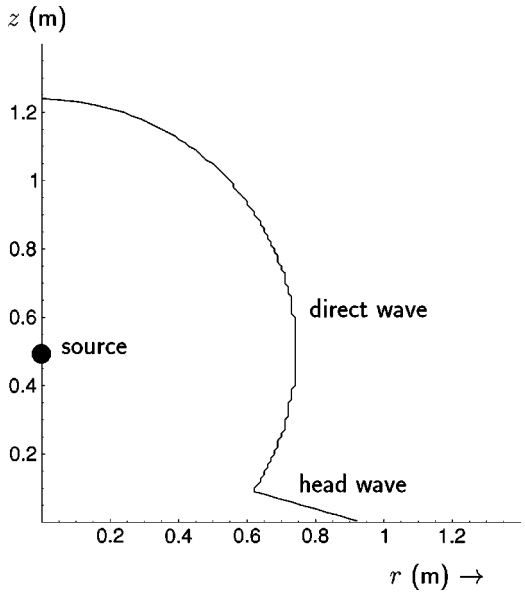

FIG. 13. Position of the wave front at $t=2.238$ ms for the case $c_1=330$ m/s, $c_2=1200$ m/s. Source is located at $r=0$ m, $z=0.5$ m.

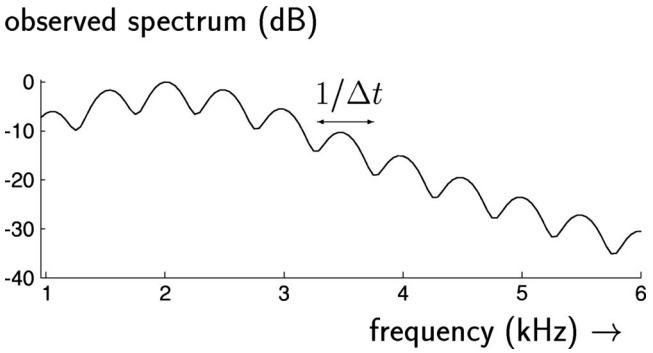

FIG. 14. Part of the observed normalized power spectrum for on-axis observation. Source is located at $r=0$ m, $z=0.25$ m, and the observation point is at $r=0$ m, $z=1.25$ m. Wave speeds are $c_1=250$ m/s, $c_2=800$ m/s. Resulting time delay between the arrivals of the direct wave and the reflected wave is $\Delta t=2$ ms. As mentioned in Sec. VI, the spacing between the minima should be $1/\Delta t=0.5$ kHz, as is indeed the case. Source parameters are $\omega_0=4\pi\times10^3$ rad s^{-1}, $\nu=2$, $\alpha=8.71\times10^3$ s^{-1}, $t_r=0.23$ ms, and $t_w=0.42$ ms.

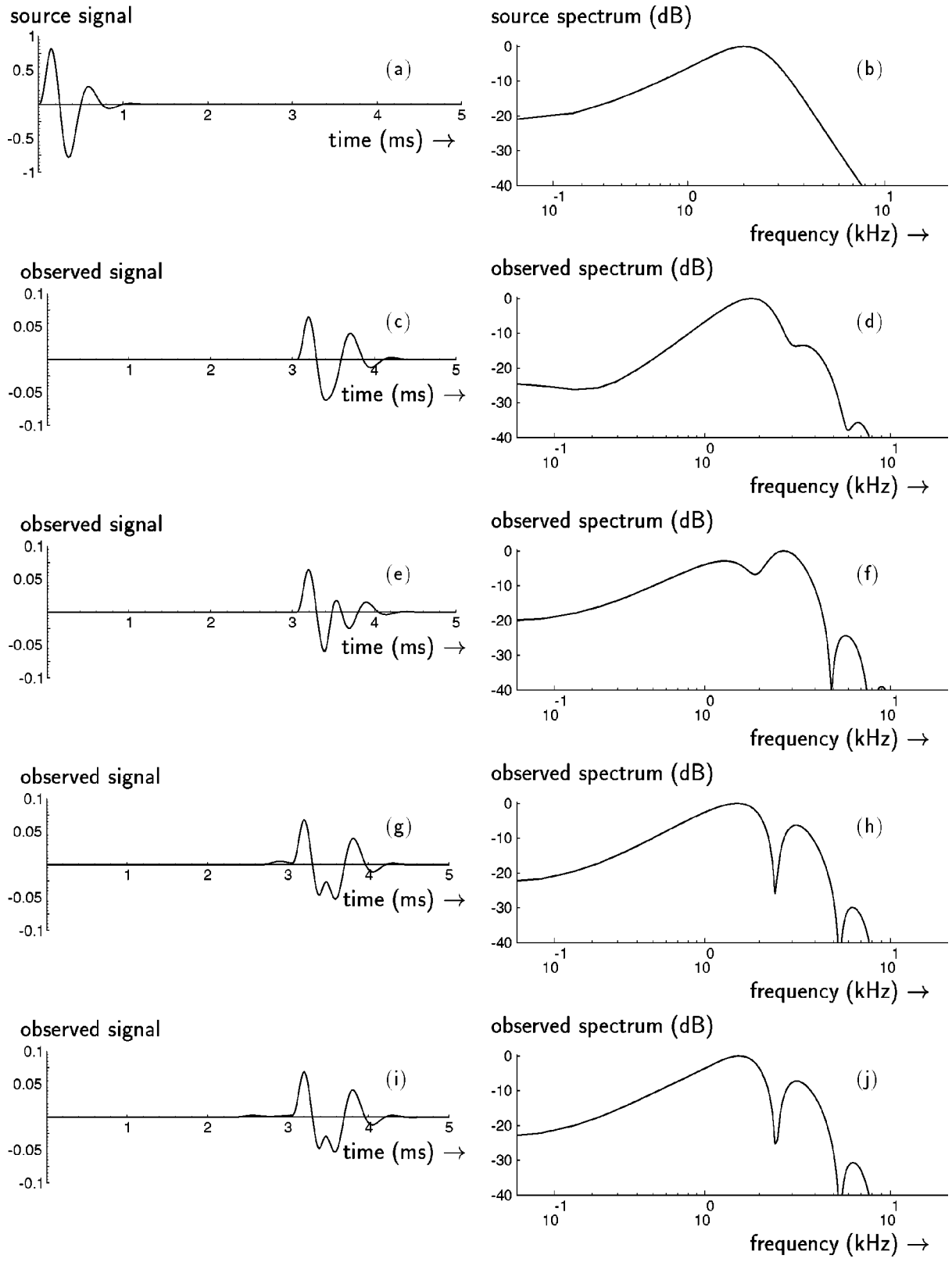

FIG. 15. Source signal (a) and its normalized power spectrum (b). Observed signal and its corresponding power spectrum are shown for different wave speeds in the second medium. In all cases $c_1=330$ m/s, arrival time of the direct wave is $\tau=3.05$ ms, and arrival time of the reflected body wave is $\tau=3.39$ ms. For $c_2=200$ m/s, there are no head waves (c,d); for $c_2=400$ m/s, the head waves arrive at $\tau=3.36$ ms (e,f); for $c_2=800$ m/s, the head waves arrive at $\tau=2.63$ ms (g,h); for $c_2=1200$ m/s, the head waves arrive at $\tau=2.29$ ms (i,j). Source parameters are $\omega_0/2\pi=2\times10^3$ rad s^{-1}, $\nu=2$, $\alpha=8.71\times10^3$ s^{-1}, $t_r=0.23$ ms, and $t_w=0.42$ ms. Source is located at $r=0$ m, $z=0.3$ m and the observation point is at $r=1.0$ m, $z=0.2$ m.

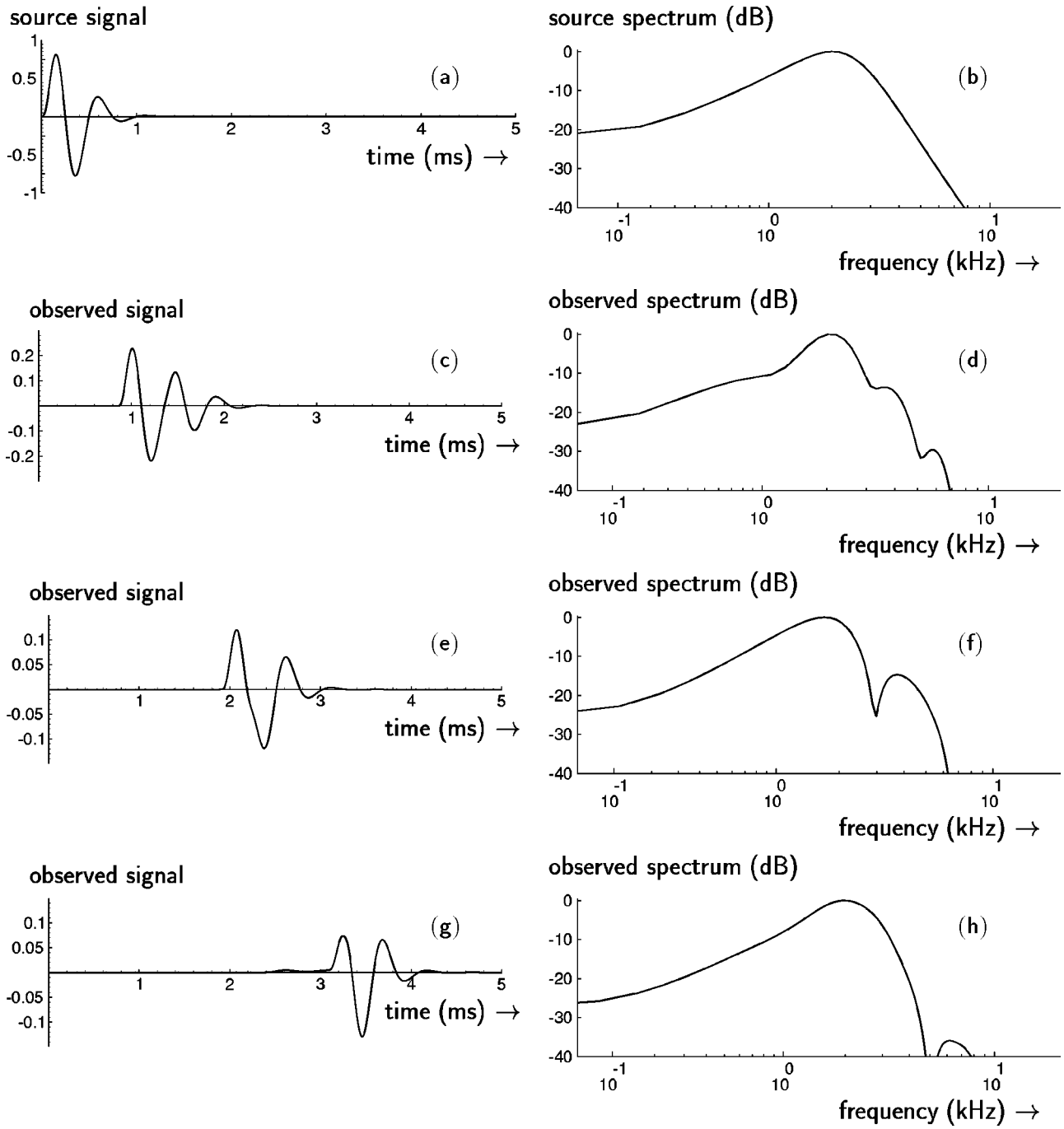

FIG. 16. Source signal (a) and its normalized power spectral density (b). Observed signal and its corresponding power spectral density are shown for different observation points in the first medium. Observation point at $r=0.2$ m, $z=0.1$ m. Head-wave, direct-wave, and body-wave arrival times are 1.35 ms, 0.86 ms, and 1.36 ms, respectively (c,d). Observation point at $r=0.6$ m, $z=0.1$ m. Head-wave, direct-wave, and body-wave arrival times are 1.85 ms, 1.92 ms, and 2.19 ms, respectively (e,f). Observation point at $r=1.0$ m, $z=0.1$ m. Head-wave, direct-wave, and body-wave arrival times are 2.35 ms, 3.09 ms, and 3.26 ms, respectively (g,h). In all cases $c_1=330$ m/s, $c_2=800$ m/s. Source is located at $r=0$ m, $z=0.3$ m. Its parameters are those of Fig. 15.

wave front. It was verified that the sine of the angle between the head wave front and the interface indeed equals c_1/c_2.

As a further test we examined the observed power spectrum under on-axis propagation and reflection. The result, shown in Fig. 14, reproduces the well-known effect from spectral interferometry [23]: the minima are equally spaced and the spacing between them equals $1/\Delta t$, where Δt is the time delay between the arrival times of the direct field and the reflected field. The spacing was found to be in excellent agreement with this prediction.

How the observed signal can differ from the signal that is emitted by the source is illustrated by Fig. 15. The source signal and its normalized power spectrum are shown in (a,b). The observation point is kept fixed and c_2, the wave speed in

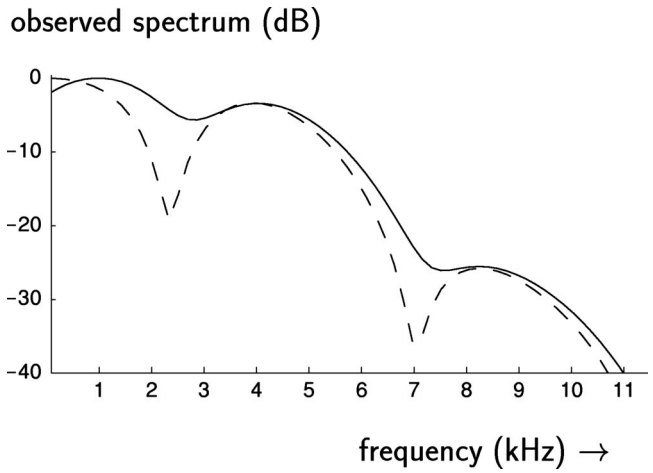

FIG. 17. Observed normalized power spectrum according to the modified Cagniard method [solid line, Eq. (48)] and the short-pulse approximation [dashed line, Eq. (83)]. The point of observation is at $r=0.3$ m, $z=0.05$ m. Wave speeds are $c_1=330$ m/s, $c_2=507$ m/s. Source is located at $r=0$ m, $z=0.3$ m. Its parameters are $\alpha=36.71\times10^3$ s^{-1}, $\nu=6$, and $\omega_0/2\pi=2$ kHz.

the medium against which reflection takes place, is varied. Changing c_2 varies the values of the reflection coefficient $\mathcal{R}$ and the arrival time of (possible) head waves. Even when no head waves are present (c,d), the observed normalized power spectrum differs significantly from that of the source. Upon increasing c_2, the interplay between head wave, body wave, and direct wave alters the shape of the observed signal and its power spectrum even more (e). It is noted that the maximum of the power spectrum is no longer at the carrier frequency $\omega_0/2\pi$ (f). In the cases (e,f) the head wave arrives after the direct wave. Upon further increasing c_2 the arrival time of the head waves decreases, and they arrive earlier than the direct wave (g,i). Also, the indentations in the observed power spectrum become much more pronounced (h,j).

The dependence of the observed power spectrum on the position of the point of observation is illustrated in Fig. 16. In this example the source signal and its power spectrum are again those of Fig. 15. Upon changing the point of observation, the arrival times of the direct, head, and body waves are altered. Also, the time delay between them changes. Even for an observation point relatively close to the source (c,d) the observed power spectrum already differs significantly from the source spectrum. When the point of observation is moved away from the source, the onset of the head wave takes place earlier (e,g), and the observed spectra (f,h) deviate even more from the emitted spectrum (b).

We emphasize that the spectral changes that we have calculated cannot be attributed to any of the four other mechanisms that are mentioned in Sec. I but are purely reflection induced.

VII. SHORT-PULSE APRROXIMATION

For short source pulses, i.e., for pulses whose spatial extent is small compared to the other spatial distances involved, we can approximate the body-wave time-domain reflection function in the final time convolution of the total wave motion by its value at the arrival time of the reflected wave. Correspondingly, the reflected wave function is approximated by

$$u_1 \simeq \mathcal{R}(rT_1/R_1^2,0)\frac{f(t-T_1)}{4\pi R_1} \tag{80}$$

(''first-motion approximation''), in which $R_1=(r^2+H_1^2)^{1/2}$ is the distance from the point of observation to the image of the source in the reflecting boundary and $T_1=R_1/c_1$ is the arrival time of the reflected body wave [cf. Eq. (44) for $q=0$]. Together with Eq. (8) we then have

$$u \simeq \frac{f(t-T_0)}{4\pi R_0} + \mathcal{R}(rT_1/R_1^2,0)\frac{f(t-T_1)}{4\pi R_1}, \tag{81}$$

in which $T_0=R_0/c_1$ is the arrival time of the direct wave. With this result we have

$$\hat{u}(s) \simeq \hat{f}(s)\left[\frac{\exp(-sT_0)}{4\pi R_0} + \mathcal{R}(rT_1/R_1^2,0)\frac{\exp(-sT_1)}{4\pi R_1}\right]. \tag{82}$$

From this, the quantity needed for the spectral diagram follows as

$$|\hat{u}(i\omega)|^2 \simeq |\hat{f}(i\omega)|^2\left\{\left(\frac{1}{4\pi R_0}\right)^2 + \left(\frac{\mathcal{R}(rT_1/R_1^2,0)}{4\pi R_1}\right)^2 + 2\left(\frac{1}{4\pi R_0}\right)\left(\frac{\mathcal{R}(rT_1/R_1^2,0)}{4\pi R_1}\right)\cos[\omega(T_1-T_0)]\right\}. \tag{83}$$

It is noted that the short-source-pulse approximation is in accordance with ray-theoretical results in that the pertinent amplitude of the reflected body wave is given by the Fresnel reflection coefficient at the reflection point at the boundary in accordance with Snell's law, while showing the divergence factor associated with the point source's image in the boundary. As such it is of heuristic value. However, beyond the range of validity of the relevent approximation the complete, exact theory as developed in this paper has to be used. As an example of such a case, we consider the spectral diagram of the total wave for a source pulse with a pulse time width $t_w=0.169$ ms. Exact results and the predictions of the short-source-pulse approximation are shown in Fig. 17. Even though the pulse time width is considerably less than the direct-wave arrival time ($T_0^{dir}=1.18$ ms) it is seen that the short-pulse approximation is in very poor agreement with the exact result as obtained with the modified Cagniard formalism.

VIII. CONCLUSIONS

We have calculated the effect of reflection on the field of a pulsed point source using the modified Cagniard technique. It is found that the observed power spectrum can differ significantly from the power spectrum that is emitted by the source. Both its shape and the position of its maximum alter. The observed spectrum depends strongly on the wave speed of the medium in which the source is embedded and that of the half space at which the field is reflected. Also, the location of the point of observation affects the spectrum.

ACKNOWLEDGMENTS

T.D.V. wishes to thank Hans van den Berg of Wageningen University and Bert Jan Kooij of Delft University of Technology for stimulating discussions. The authors thank Michiel Min for his technical assistance.

[1] J. van Bladel, *Relativity and Engineering* (Springer, Berlin, 1984). See, in particular, Chap. 5.
[2] K. E. Oughstun and G. C. Sherman, *Electromagnetic Pulse Propagation in Causal Dielectrics* (Springer, Berlin, 1997).
[3] M. F. Bocko, D. H. Douglass, and R. S. Knox, Phys. Rev. Lett. **58**, 2649 (1987).
[4] L. Mandel and E. Wolf, *Optical Coherence and Quantum Optics* (Cambridge University Press, Cambridge, 1995).
[5] E. Wolf and D. F. V. James, Rep. Prog. Phys. **59**, 771 (1996).
[6] A. T. de Hopp, Appl. Sci. Res., Sect. B **8**, 349 (1960).
[7] A. T. de Hoop and H. J. Frankena, Appl. Sci. Res., Sect. B **8**, 369 (1960).
[8] A. T. de Hoop, Radio Sci. **14**, 253 (1979).
[9] A. T. de Hoop and J. H. M. T. van der Hijden, J. Acoust. Soc. Am. **74**, 333 (1984).
[10] A. T. de Hoop and J. H. M. T. van der Hijden, J. Acoust. Soc. Am. **75**, 1709 (1984).
[11] A. T. de Hoop and J. H. M. T. van der Hijden, Geophysics **50**, 1083 (1985).
[12] J. H. M. T. van der Hijden, *Propagation of Transient Elastic Waves in Stratified Anisotropic Media* (North-Holland, Amsterdam, 1987).
[13] A. T. de Hoop, ''Acoustic Radiation from Impulsive Sources in a Layered Fluid,'' Nieuw Arch. Wis., Vierde Ser. **6**, 111 (1988).
[14] A. T. de Hoop, J. Acoust. Soc. Am. **88**, 2376 (1990).
[15] M. D. Verweij, J. Acoust. Soc. Am. **92**, 2223 (1992).
[16] M. D. Verweij and A. T. de Hoop, in *Computational Acoustics*, Vol. 1, edited by R. L. Lau, D. Lee, and A. R. Robinson (Elsevier, Amsterdam, 1993).
[17] H. J. Stam, Geophysics **55**, 1047 (1990).
[18] A. T. de Hoop, S. Zeroug, and S. Kostek, J. Acoust. Soc. Am. **98**, 1767 (1995).
[19] D. V. Widder, *The Laplace Transform* (Princeton University Press, Princeton, NJ, 1946).
[20] H. Maecker, Ann. Phys. (Leipzig) **6**, 28 (1949).
[21] L. Mintrop, *Zur Geschichte des seismischen Verfahrens zur Erforschung von Gebirgsschichten und Nutzbaren Lagerstätten*, Mitteilungen der Seismos-Gesellschaft II (Seismos, Hannover, 1930).
[22] NAG FORTRAN Library Mark 17, Numerical Algorithm Group Ltd., Oxford, U.K.
[23] I. A. Walmsley, Opt. Photonics News **10**, 28 (1999), and references therein.